Journal of Materials Chemistry C

ROYAL SOCIETY OF CHEMISTRY

PAPER

View Article Online
View Journal | View Issue

Cite this: J. Mater. Chem. C, 2025, 13, 8544

UV to NIR photodetection in lateral homojunction PN diode of WSe_2 achieved *via* IGZO sputtering†

Muhammad Abubakr,‡[ab] Muhammad Hamza Pervez, ‡[c] Arslan Rehmat,‡[d] Muhammad Asghar Khan,[d] Ehsan Elahi, [e] Muhammad Asim,[d] Muhammad Rabeel,[b] Muhammad Nasim,[c] Zeesham Abbas,[f] Malik Abdul Rehman,[g] Aize Hao, [h] Jonghwa Eom, [d] Shania Rehman *[c] and Muhammad Farooq Khan *[i]

Nano-devices based on two-dimensional (2D) semiconductor materials encourage the development of high-performance homogeneous junctions owing to their remarkable electronic and optoelectronic properties. Herein, we fabricated an atomically thin WSe_2 (~4.8 nm) lateral homojunction PN diode through the deposition of indium gallium zinc oxide (IGZO) *via* sputtering. Pristine WSe_2 exhibited dominant p-type semiconductor behavior, while IGZO-deposited WSe_2 demonstrated n-type behavior, revealing that IGZO altered the carrier polarity of WSe_2 from p- to n-type. Furthermore, we investigated gate-dependent I–V curves of the lateral homojunction PN (p-WSe_2/n-IGZO·WSe_2) diode in the dark based on a single WSe_2 flake, which showed a promising current rectification ratio (~1.6×10^4) and ideality factor (~1.23) at V_{BG} = −30 V, respectively. Subsequently, to explore the photodiode characteristics, we irradiated the lateral homojunction PN diode of WSe_2 under ultra-violet (UV) to near-infrared (NIR) light (365, 530, and 850 nm). The I–V curves of the diode significantly changed under light irradiation, and the open circuit voltage (V_{oc} = 202, 166, and 134 mV) and short circuit current (I_{sc} = 320, 171, and 122 nA) values increased under illumination of a laser of small wavelength (365, 530, and 850 nm). Furthermore, we investigated the time-dependent photoresponse behavior of the diode under different laser lights. This demonstrated promising photoresponsivity (R_{Ph} = 40.1 A W^{-1}) and external quantum efficiency (EQE = 13 634%) at λ = 365 nm and V_{BG} = 15 V. Hence, our lateral homojunction PN diode WSe_2–IGZO/WSe_2 shows great potential for next-generation electronic devices at the nanoscale level.

Received 6th November 2024,
Accepted 11th March 2025

DOI: 10.1039/d4tc04705b

rsc.li/materials-c

1. Introduction

In the ever-evolving landscape of semiconductor materials and device technology, the quest for innovative strategies to manipulate material properties remains continues relentlessly. Two-dimensional (2D) materials offer immense potential for the advancement of next generation electronic and optoelectronic technological innovations.[1,2] Various 2D materials, especially transition metal dichalcogenides (TMDCs), have garnered significant attention owing to their atomic thickness, tunable energy bandgap, mechanical flexibility and dangling bond free surface.[3–6] The versatility of 2D materials offers a fascinating prospect for electronic and optoelectronic applications as high mobility field-effect transistors (FETs), PN diodes, memory devices, logic gates and optical imaging and communication.[7–10] Moreover, 2D materials provide significant liberty to architect novel PN junction devices that could compete with conventional bulk semiconductor diodes. Recently, several homo- and hetero-junction PN junctions, including mixed dimensional junctions of

[a] Department of Materials Engineering and Convergence Technology, Gyeongsang National University, Jinju, Gyeongsangnam-do 52828, Republic of Korea
[b] Department of Electrical Engineering, Sejong University, Seoul, 05006, Republic of Korea
[c] Department of Semiconductor Systems Engineering, Sejong University, Seoul, 05006, Republic of Korea. E-mail: shania.rehman19@sejong.ac.kr
[d] Department of Physics & Astronomy, Sejong University, Seoul, 05006, Republic of Korea
[e] Department of Inorganic Chemistry, University of Chemistry and Technology Prague, Prague 616628, Czech Republic
[f] Department of Nanotechnology and Advanced Materials Engineering, Sejong University, Seoul, 05006, Republic of Korea
[g] Department of Chemical Engineering, New Uzbekistan University, Tashkent 100007, Uzbekistan
[h] College of Chemical Engineering, Sichuan University of Science and Engineering, Zigong 643000, Sichuan, P. R. China
[i] Department of AI Convergence Electronic Engineering, Sejong University, Seoul, 05006, Republic of Korea. E-mail: mfk@sejong.ac.kr

† Electronic supplementary information (ESI) available. See DOI: https://doi.org/10.1039/d4tc04705b

‡ These authors contributed equally.

2D materials, have been established for various ultra-fast programmable applications.[11–13] In recent research, homojunction and heterojunction diodes of 2D TMDC semiconductor materials were explored. For example, a vertically stacked heterojunction of MoS_2 and BP showed 70 times higher current density compared with lateral configuration.[14] In contrast, a homojunction PN diode of $MoTe_2$ exhibited tremendous rectification with a promising ideality factor ($\sim$1.05), demonstrating excellent interface quality.[15] Both homojunction and heterojunction PN diodes have demonstrated a high current rectification ratio without the application of an electric field. Homojunctions have the advantage of reduced interface traps, while heterojunctions provide a broad range of material selection and facile approach of self-encapsulation to circumvent the oxidation process.[14] Homojunction diodes also generally offer several advantages, including the ability to establish a rapid junction interface and maintain a stable electric field through electrostatic doping and thickness modulation.[16–18] These features enable continuous tuning of band alignments using back-gate voltage, providing flexibility in controlling interfacial energy-band profiles, carrier transport, and photoelectric conversion.[19,20] These attributes make homojunction diodes an indispensable element for heterogeneous integration to advance electronic and optoelectronic applications.

Herein, we present a facile approach to engineer WSe_2, converting its intrinsic p-type semiconductor behavior into n-type by depositing IGZO *via* sputtering, thereby creating a versatile PN diode configuration. This remarkable achievement was realized through the controlled doping of WSe_2 with IGZO. The established lateral homojunction PN (p-WSe_2/n-IGZO·WSe_2) diode based on a single WSe_2 flake demonstrated excellent photodetection capabilities across a broad spectrum, encompassing ultraviolet (UV = 365 nm) to near-infrared (NIR = 850 nm) regions. In addition, we assessed the key performance metrics, including photoresponsivity and EQE, under varying illumination conditions and back-gate voltages. Remarkably, the device exhibited outstanding PN photodiode characteristics, thus offering potential applications in photodetectors, light-emitting diodes, logic invertors and optical sensors.

2. Materials and methods

2.1. Device fabrication

WSe_2 bulk crystals were purchased from HQ Graphene, and ultrathin WSe_2 nanoflakes were obtained through mechanical exfoliation in a cleanroom environment using adhesive tape. A dry transfer method, utilizing a micromanipulator and a transparent PDMS stamp, was employed to stack WSe_2 onto an SiO_2/Si substrate (SiO_2 = 300 nm) within a 90 $\times$ 90 μm^2 window of a large pattern. Following the transfer, the substrate underwent a heat treatment on a hot plate at 90 °C to eliminate residual water vapors. Throughout the process, the samples underwent sequential cleaning steps with acetone and methanol, followed by drying with nitrogen gas flow. For electrode nanofabrication, a standard e-beam lithography procedure was executed to create patterns for the source/drain electrodes. Metal contacts (Cr/Au, 8/80 nm thickness) were deposited using the thermal evaporation process. Subsequently, a window was designed on the WSe_2 flake through e-beam lithography before the deposition of IGZO. Finally, IGZO was deposited onto the WSe_2 flake and a lift-off process was accomplished using acetone and methanol to ensure that the deposition was performed on the required area. For deposition of IGZO, the base pressure in the chamber was maintained at 2.2 $\times$ 10^{-6} torr. Argon (9.0 sccm) and oxygen (1.0 sccm) gases were used for plasma. The deposition was performed using RF magnetron sputtering at a constant sputtering power of 100 W and room temperature.

2.2. Material and device characterization

The band structural study of WSe_2 flake was carried out by Raman spectroscopy (Renishaw, InVia systems) at room temperature by keeping the laser wavelength at 514 nm. The laser power was fixed at 1.0 mW to prevent heating effect. The thickness of WSe_2 flake and IGZO thin film was measured by atomic force microscopy (AFM, Nano focus Inc.). In addition, the electrical measurements were conducted in a vacuum box using a source meter (Keithley 2400) and pico-ammeter (Keithley 6485). All photovoltaic measurements were performed with lasers ranging from 350–850 nm by adjusting the light intensity accordingly.

3. Results and discussion

A schematic representation of the fabricated FET is illustrated in Fig. 1a, with separate source (S) and drain (D) electrodes for WSe_2 and IGZO/WSe_2 FETs on Si/SiO_2 substrate. By utilizing the mechanical exfoliation technique, WSe_2 nanoflakes were exfoliated and these nanoflakes were subsequently transferred onto a Si/SiO_2 substrate using a polydimethylsiloxane (PDMS) stamp, followed by the deposition of Cr/Au electrodes with thicknesses of 3 and 80 nm, respectively. Fig. 1b presents the original optical microscope image of the fabricated device. The region outlined by the red dotted line highlights the WSe_2 flake along with the source and drain electrodes, while the blue dotted region indicates the area where IGZO has been deposited. The thickness of the WSe_2 flake and IGZO was verified using atomic force microscopy (AFM), as presented in Fig. 1c. The AFM measurements, conducted in non-contact mode under ambient conditions, revealed a uniform and homogeneous surface morphology, with a thickness of approximately $\sim$4.8 and $\sim$15 nm for WSe_2 and IGZO, respectively, as shown in the thickness profile in Fig. 1d and e. Furthermore, Raman spectroscopy was employed to investigate the vibrational characteristics of the WSe_2 flake. The spectrum, presented in Fig. S1 (ESI†), exhibits characteristic peaks at 250 cm^{-1} (E^1_{2g} mode), and 260 cm^{-1} (A_{1g} mode), which are in good agreement with previously reported data in the literature.[21]

To assess the electrical performance of the fabricated devices, transfer curve measurements (I_{ds}–V_{BG}) were conducted at V_{ds} = 0.5 V for pristine WSe_2 and IGZO/WSe_2 FETs, as shown in Fig. 2a and b.

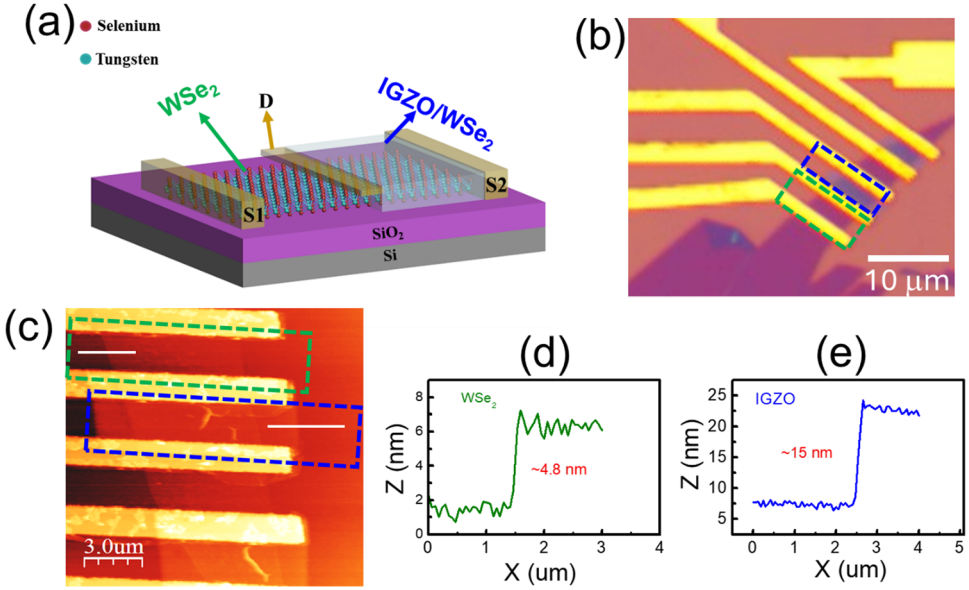

Fig. 1 (a) Schematic of the fabricated WSe_2 and IGZO/WSe_2 FETs. (b) Optical microscopy image of the WSe_2 flake with IGZO deposition on the Si/SiO_2 substrate. (c) AFM image of the IGZO and WSe_2 thin film. (d) Height profile of the WSe_2 flake and (e) IGZO.

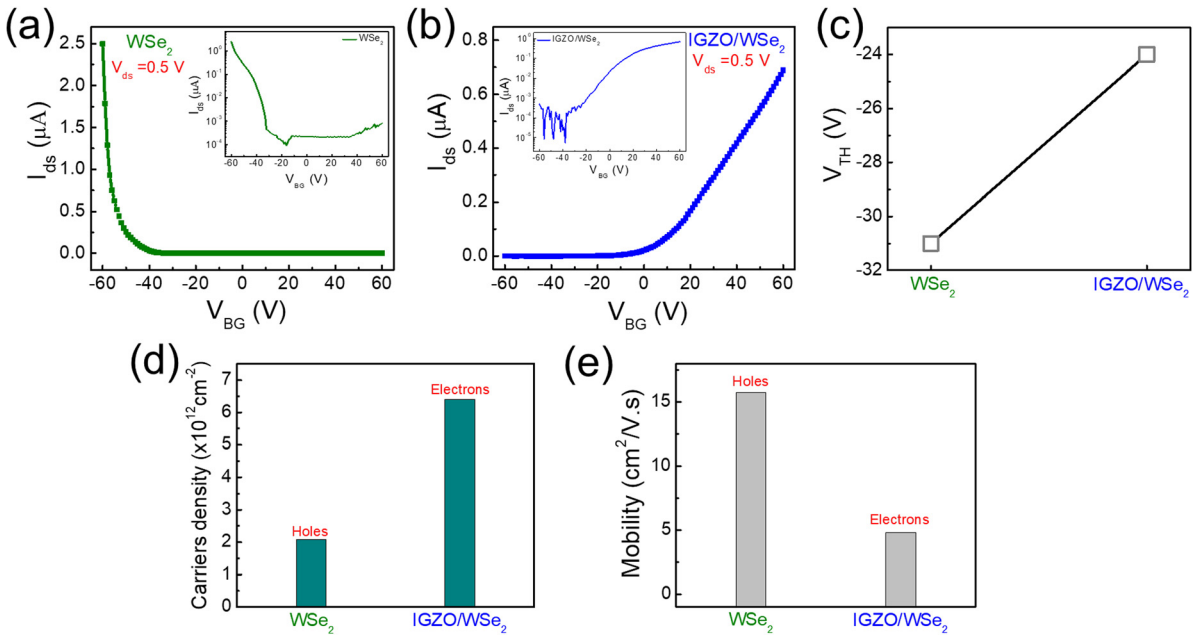

Fig. 2 (a) and (b) Transfer curves (I_{ds}–V_{BG}) with logarithmic insets. (c) Threshold voltage, (d) carrier concentration, and (e) field-effect mobility of electrons and holes of WSe_2 and IGZO/WSe_2.

The pristine WSe_2 device exhibited dominant p-type behavior, as evidenced by its transfer characteristics. Following the deposition of a 15 nm IGZO layer, a significant shift in the threshold voltage and a clear transition to n-type conduction were observed, validating the electron doping effect induced by sputtered IGZO. These results indicate that the IGZO layer effectively modulated the carrier polarity of WSe_2 from p-type to n-type, demonstrating the feasibility of controlled n-type doping through IGZO sputtering. In addition, the individual IGZO thin film transistor characteristics with intended controlled sputtering conditions showed its oxide behavior rather than semiconductor nature, as shown in Fig. S2 (ESI†). Thus, the observed n-type behavior is likely from only the WSe_2 flake attributed to the electron doping effect by sputtered IGZO. Fig. 2c presents the threshold voltage (V_{TH}) for the WSe_2 and IGZO/WSe_2 FETs *i.e.*, −31 V and −24 V, respectively, demonstrating that the IGZO/WSe_2 configuration exhibits a higher threshold voltage compared with WSe_2 alone.

Moreover, the carrier's density/concentration (n) of holes and electrons at V_{BG} = −60 V and V_{BG} = +60 V for WSe_2 and IGZO/WSe_2 was calculated to be 2.08 × 10^{12} cm^{-2} and 6.4 × 10^{12} cm^{-2}, respectively, using the following eqn (1):[22]

$$n = \frac{C_g(V_g - V_{th})}{e}, \quad (1)$$

where C_g, V_g, V_{th}, and e refer to capacitance, gate voltage, threshold voltage, and electronic charge, respectively. As depicted in Fig. 2d, a significant variation in carrier concentration was observed while comparing the WSe_2 and IGZO/WSe_2 FETs. For pristine WSe_2, the hole carrier density (n_h) was notably higher than the electron carrier density (n_e), which was consistent with the material's intrinsic p-type nature. The integration of IGZO, however, resulted in a pronounced shift in carrier concentration, with a substantial increase in electron density and a corresponding decrease in hole density. This rise in electron carriers highlights the critical function of IGZO in promoting electron transfer to WSe_2. The shift in carrier concentrations induced by IGZO doping further confirms its efficacy in altering charge carrier dynamics within the WSe_2 material, thereby illustrating its capacity to enable precise and efficient control over the material's electrical properties.

We also calculated the field-effect mobility for WSe_2 and IGZO/WSe_2 FETs using eqn (2):[23]

$$\mu_{FET} = \frac{1}{C_g}\cdot\frac{1}{V_{ds}}\left[dI_{ds}/dV_g(L/W)\right] \quad (2)$$

The parameters C_g, V_{ds}, dI_{ds}/dV_g, L, and W represent the gate capacitance, drain–source voltage, transconductance (slope of the I_d–V_g curve), channel length, and channel width, respectively. From Fig. 2e it is evident that the hole mobility (~16 cm^2 V^{-1} s^{-1}) is notably higher than the electron mobility in WSe_2. Conversely, in IGZO/WSe_2 the mobility of electrons (~5 cm^2 V^{-1} s^{-1}) surpasses that of holes.

Fig. 3a shows the structure presented in a schematic diagram which demonstrates the integration of WSe_2 as the p-type channel and IGZO·WSe_2 as the n-type material, fabricated on a SiO_2 substrate. The back-gate dependent (−30, −20, −10, 0, +10 V) output characteristics (I_{ds}–V_{ds}) of homo-PN diode of n-WSe_2/p-IGZO·WSe_2 has been shown in Fig. 3b. The semi-logarithmic plot of diode behavior is depicted in detail in Fig. 3c, which shows a substantial reduction in leakage current with more negative V_{BG}, resulting in a high on/off current ratio, indicating strong gate control. To assess the stability and reliability of the fabricated device, we subjected it to prolonged exposure under ambient environmental conditions. After an interval of two months, we rechecked the device output characteristics (I_{ds}–V_{ds}) to monitor any changes in its electrical performance. As shown in Fig. S3 (ESI†), the device exhibits almost similar behavior, indicating robust stability over time.

The rectification ratio (RR), defined as I_{ON}/I_{OFF}, increases with more negative V_{BG}, reaching approximately ~10^4 at V_{BG} = −30 V (Fig. 3d). This gate-dependent RR reflects the transistor's optimal performance in the p-type regime, making it suitable for rectifying applications.

We also calculated evaluated the ideality factor by using the ideal diode equation:[24–26]

$$I = I_{sat}\left[\exp\left(\frac{V}{nV_t}\right) - 1\right] \quad (3)$$

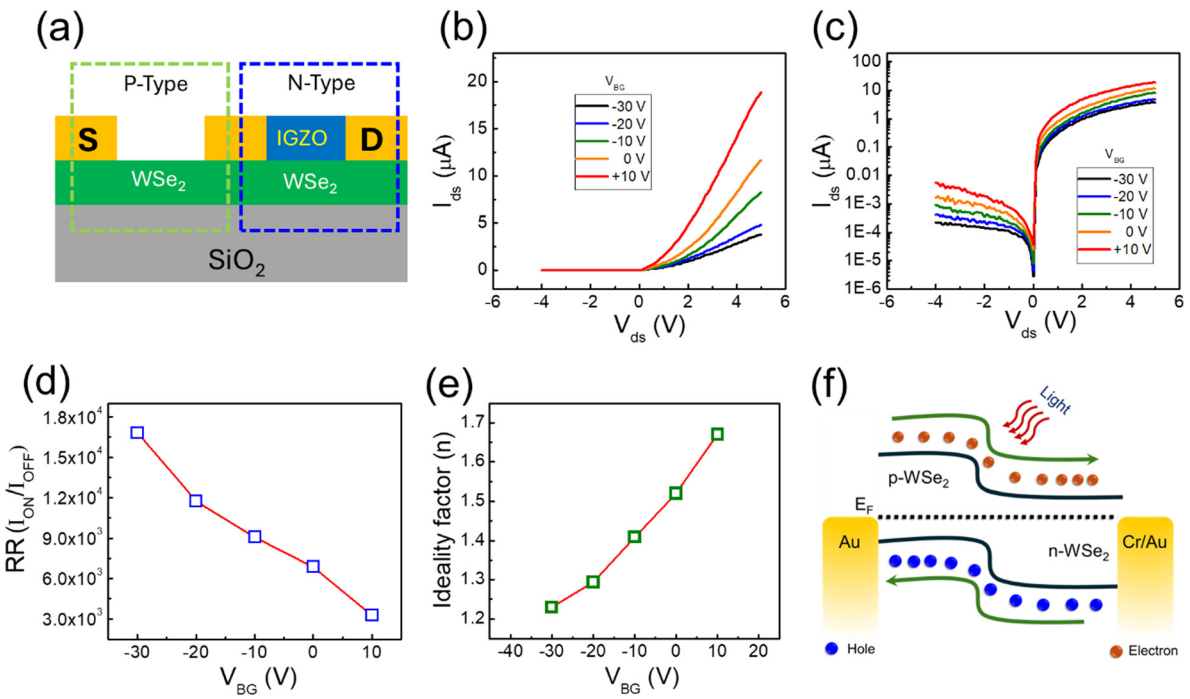

Fig. 3 (a) Schematic of the fabricated device indicating p-type and n-type regions for WSe_2 and IGZO/WSe_2, respectively. (b) Gate dependent I–V curves on a linear scale. (c) Output characteristics (I_{ds}–V_{ds}) of the homo-PN diode (p-WSe_2/n-IGZO·WSe_2) on a logarithmic scale. (d) Rectification ratio (RR) of the homo-PN diode. (e) Ideality factor of the homo-PN diode. (f) Energy band diagram of the WSe_2 p–n homojunction under light.

where I, I_{sat}, V, n, and V_t are the current through the diode, reverse-bias saturation current, voltage across the diode, ideality factor, and thermal voltage (25.9 mV), respectively. Under the forward bias voltage of greater than a few millivolts, the above equation can be rewritten as:[27]

$$I = I_{sat} \exp\left(\frac{V}{nV_t}\right) \quad (4)$$

The ideality factor, shown in Fig. 3e, varies with V_{BG}, ranging from ~1.2 at −30 V to ~1.7 at +10 V. A lower ideality factor in the p-type regime suggests a near-ideal diode-like behavior, while the higher values in the n-type regime may indicate increased recombination or trap states in IGZO. The fabricated FET demonstrates strong potential for multifunctional devices, with its tunable ambipolar conduction, high RR, and adjustable ideality factor. Further, to understand the energy band alignment under light for p-WSe_2 and n-WSe_2, we provide a schematic illustration as depicted in Fig. 3f.

To elucidate broadband photodetection, we illuminated the homodiode device under light, as illustrated in Fig. 4a. We measured output characteristics (I_{ds}–V_{ds}) under light in a vacuum, as shown in Fig. 4b. We illuminated the homodiode at different wavelengths varying from UV to NIR (365, 530 and 850 nm) with a fixed gate voltage (V_{BG}) of 20 V and intensity of 50 mW cm^{-2}. Under dark conditions, minimal drain–source current (I_{ds}) is exhibited by the device, which indicates low carrier generation. However, upon illumination, I_{ds} increases significantly, particularly at shorter wavelengths, as evidenced by the pronounced rise in current value at 365 nm. This behavior highlights the wavelength-dependent photoresponse of the homodiode (p-WSe_2/n-IGZO·WSe_2), where shorter wavelengths generate more charge carriers due to higher photon energy. The enhanced photocurrent at shorter wavelengths suggests strong absorption in the ultraviolet-visible spectrum, making the device suitable for UV-visible photodetection.

A more detailed view of the diode behavior at low bias is presented in Fig. 4c, where the current response near zero bias is plotted. Under illumination, a clear photoconductive effect is observed, with the photocurrent increasing as the wavelength decreases. The 365 nm illumination produces the highest photocurrent, followed by 530 nm and 850 nm. The significant modulation of I_{ds} near zero bias further demonstrates the device's sensitivity to light, particularly at UV wavelengths. This strong photocurrent response at shorter wavelengths suggests that the homojunction structure efficiently separates and collects photo-generated carriers, even at low bias conditions.

The photovoltaic properties of the device are characterized by the open-circuit voltage V_{OC} and short-circuit current I_{SC}, as shown in Fig. 4d and e, respectively. The V_{OC}, plotted in Fig. 4d, decreases with increasing wavelength, from approximately 200 mV at 365 nm to around 130 mV at 850 nm. This trend is consistent with the fact that higher-energy photons (shorter wavelengths) generate more photo-excited carriers, leading to a higher photovoltage. As the wavelength increases, the lower photon energy results in fewer generated carriers and, thus, a reduction in V_{OC}. Similarly, the short-circuit current I_{SC}, shown

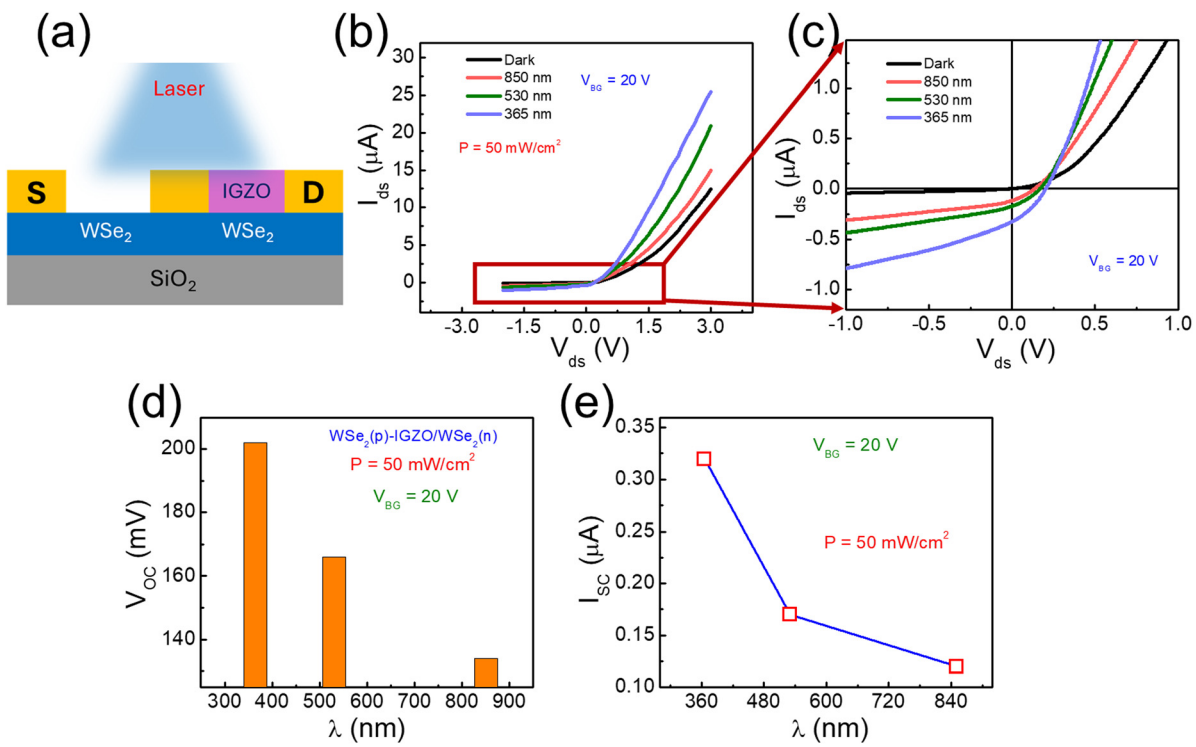

Fig. 4 (a) Schematic of the WSe_2 and IGZO/WSe_2 devices under laser source. (b) Gate-dependent output characteristics (I_{ds}–V_{ds}) of the device under different wavelengths at V_{BG} = 20 V. (c) Enlarged view of I_{ds}–V_{ds} curves of the device. (d) and (e) Variation in the V_{OC} and I_{SC} of the device at V_{BG} = 20 V with the wavelength of illumination source at P = 50 mW cm^{-2}.

in Fig. 4e, decreases as the wavelength increases, from about 0.30 μA at 365 nm to 0.10 μA at 850 nm. This reduction in I_{SC} with increasing wavelength reflects the lower photon absorption efficiency of the homo-PN diode at longer wavelengths, which results in reduced carrier generation and collection.

The photodetection characteristics are attributed to the lateral p-WSe_2/n-IGZO·WSe_2 homojunction, where a built-in electric field at the junction efficiently separates charge carriers under illumination, leading to increased photocurrent and photovoltage with decreasing wavelength. The strong absorption of WSe_2 and effective charge transfer by IGZO doping enhance performance, ensuring minimal recombination and improved carrier transport compared to heterojunctions. The higher photocurrent at shorter wavelengths (365 nm) is due to increased photon energy, resulting in large electron–hole pair generation. These results highlight the robustness of the homojunction in achieving high responsivity across a broad light spectrum.

The time-resolved photoresponse of the (p-WSe_2/(n)IGZO-WSe_2) lateral homojunction was evaluated under illumination at three different wavelengths (365 nm, 530 nm, and 850 nm) with a constant incident power density of 25 mW cm^{-2} and a gate bias voltage of V_{BG} = +10 V, as shown in Fig. 5a. The device exhibited a clear and repeatable photocurrent response upon alternating exposure to light and dark cycles of 10 s. The magnitude of the photocurrent I_{ds} under illumination varies with wavelength, with the highest response observed at V_{BG} = +10 V, P = 25 mW cm^{-2}, for 365 nm *i.e.*, $I_{ds} \approx$ 0.21 μA, and the lowest for 850 nm *i.e.*, $I_{ds} \approx$ 0.05 μA.

A clear view of the device's photoresponse under three different wavelengths *i.e.*, 365 nm, 530 nm, and 850 nm, is depicted in Fig. 5b, which shows a response of $I_{ds} \approx$ 190 nA at P = 25 mW cm^{-2} and V_{BG} = +10 V under 365 nm wavelength. We also calculated the rise/decay times *i.e.*, ≈1.7 and 1.9 s using the following equation in order to explore the response time of the device, as shown in Fig. 5c:

$$I_t = I_{dark} + Be^{\left(-\frac{t}{\tau_d}\right)} \quad (5)$$

where I_t, I_{dark}, and τ_d relate to the currents under light and dark conditions and the decay time of devices, respectively.

To quantify the change in photocurrent ΔI_{ph} due to illumination, Fig. 5d presents a comparison of the photocurrent response at two different gate voltages *i.e.*, at V_{BG} = +10 V and V_{BG} = +15 V. It is observed that the photocurrent increases with increasing V_{BG}, which can be attributed to the enhanced electric field at higher gate biases that facilitates a more efficient separation and collection of photo-generated electron–hole pairs. As expected, shorter wavelengths (higher photon energies) result in greater ΔI_{ph}, with 365 nm illumination yielding a maximum photocurrent response of approximately 250 nA at V_{BG} = +15 V.

Photoresponsivity (R_{ph}) is a critical parameter in the evaluation of photodetectors, as it quantifies the performance of a device under incident light. We calculated this parameter by using the following equation:[28]

$$R = \frac{I_{ph}}{P \cdot A} \quad (6)$$

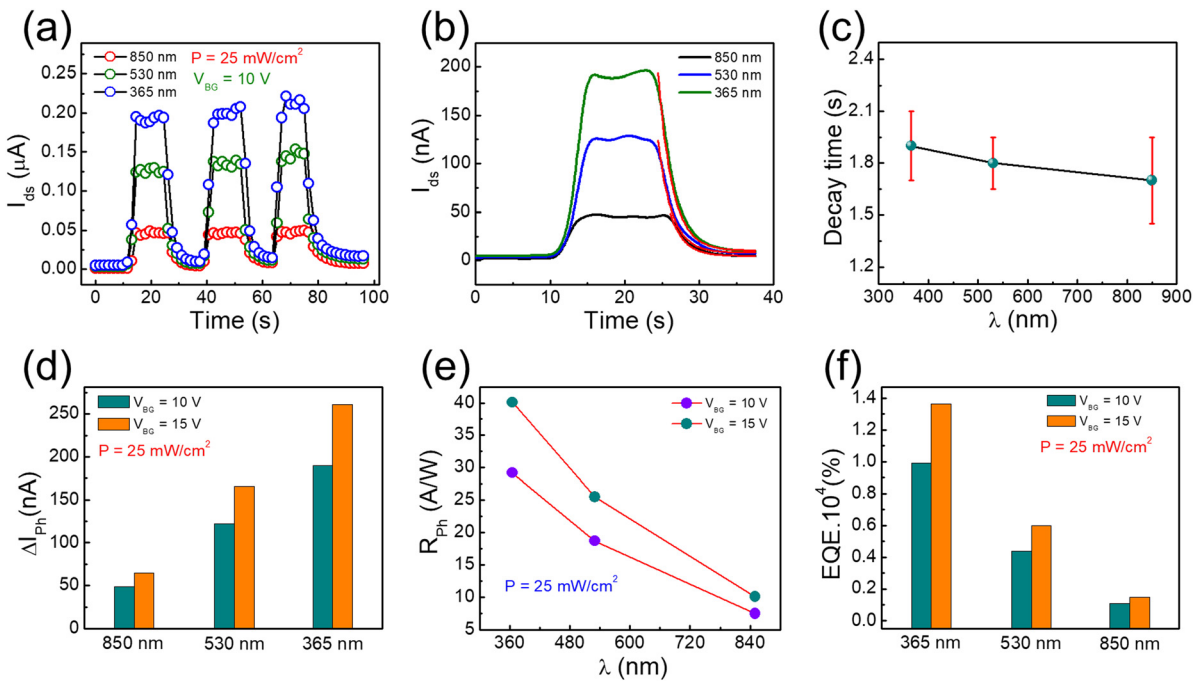

Fig. 5 (a) Time-resolved photo response of the lateral homodiode at V_{BG} = 10 V and P = 25 mW cm^{-2}. (b) Time-resolved photo response of the homojunction PN diode (p-WSe_2/n-IGZO·WSe_2). (c) Estimated decay time of p-WSe_2/n-IGZO·WSe_2 under various wavelengths of light. (d) Variation in photocurrent under different wavelengths at V_{BG} = 10 V and 15 V. (e) Variation in the photoresponsivity of the device at V_{BG} = 10 V and 15 V with the wavelength of the illumination source. (f) EQE of the devices at V_{BG}= 10 V and 15 V under 365, 530, and 850 nm wavelengths of light.

I_{ph}, P and A are photocurrent, power intensity, and active area of the device, respectively.

Fig. 5e shows the R_{ph} of the device which is plotted against different wavelengths *i.e.*, 365 nm, 530 nm, and 850 nm at V_{BG} = +10 V, and V_{BG} = +15 V, respectively. The responsivity follows a decreasing trend as the illumination wavelength increases. At 365 nm, the responsivity reaches as high as 40 A W^{-1} at V_{BG} = +15 V, which is notably higher compared to the values at 530 nm and 850 nm. The responsivity decreases sharply beyond 530 nm, reaching less than 10 A W^{-1} at 850 nm which can be attributed to the reduced optical absorption and lower generation of photo-carriers at large wavelengths, as the photon energy becomes insufficient to excite electrons across the bandgap of WSe_2.

Additionally, the external quantum efficiency (EQE), a key figure of merit for photodetectors, was calculated by using the following relation[28] and is presented in Fig. 5f.

$$\mathrm{EQE} = R\frac{hc}{e\lambda} \tag{7}$$

R, h, c, e and λ are photoresponsivity, Planck's constant, speed of light, charge, and wavelength, respectively. The EQE values exhibit a similar trend to the responsivity, with the maximum EQE observed at 365 nm for both gate voltages. At V_{BG} = +15 V, the EQE reaches over $\sim 1.3 \times 10^4$%, highlighting the high efficiency of the photodetector in converting incident photons into electrical carriers. The EQE decreases significantly as the wavelength increases, dropping to approximately 0.2×10^4% at 850 nm, reflecting the reduced photoresponse at lower photon energies. However, there is an apparent correlation between V_{GB} and photodetection performance; higher V_{BG} improves photocurrent, responsivity, and EQE at all measured wavelengths. This is probably because of the enhanced electric field across the junction, which aids in a more efficient separation of photo-generated carriers due to impact ionization process, so that the overall performance is improved. Our results present critical insights into the synergistic interactions between IGZO and WSe_2, highlighting their potential to revolutionize electronic device architectures. These findings lay a robust foundation for the future development of high-performance, energy-efficient systems, positioning IGZO/WSe_2 as a promising material platform in next-generation electronics and semiconductor technologies.

4. Conclusion

In summary, we fabricated an FET using WSe_2 thin films that intrinsically showed p-type semiconductor behavior. Subsequently, we deposited an IGZO layer on a localized part of a WSe_2 flake, which converted it from p-type to n-type. This conversion was attributed to selective electron doping of WSe_2 by IGZO. This approach helped engineer a lateral homojunction PN diode (p-WSe_2/n-IGZO·WSe_2) with a promising current rectification ratio and ideality factor due to a sharp interface between the WSe_2 and p-WSe_2 regions. Furthermore, we investigated this diode under broadband wavelengths of light and thereby demonstrated its outstanding photovoltaic property. This scheme opens up a new avenue to introduce an efficient manipulation of the carrier type in 2D materials using IGZO. Thus, this work describes a facile and non-destructive approach toward next-generation logic and CMOS inverter devices with high efficiency.

Author contributions

The manuscript was written through contributions from all the authors. All the authors have given approval to the final version of the manuscript. M. A., M. H. P., and A. R. conceived the idea, fabricated the devices and carried out the investigations. M. A. K., E. E., M. A., and M. R. conducted the analysis and measurements. M. N., Z. A., M. A. R., and A. Z. assisted in writing the initial draft of the manuscript. All co-authors assisted in writing the manuscript. J. E., S. R. and M. F. K. provided essential contributions to interpreting the results and reviewing the final manuscript. J. E. and M. F. K. supervised and provided the funding resources for this research.

Data availability

The data are available from the corresponding author upon reasonable request.

Conflicts of interest

The authors state that they have no competing financial or non-financial interests.

Acknowledgements

This work was supported by the National Research Foundation of Korea (NRF) basic research grant funded by the Korean government (MSIT) (No. 2022R1F1A1075229). This research was also supported by the MSIT (Ministry of Science and ICT), Korea, under ITRC (Information Technology Research Center) support program (IITP-2024-RS-2024-00437191) supervised by the IITP (Institute for Information & Communications Technology Planning & Evaluation). In addition, this research was partly supported by the Korea Basic Science Institute (National Research Facilities and Equipment Center) grant funded by the Ministry of Education. (No. 2022R1A6C101A774).

References

1 C. Liu, H. Chen, S. Wang, Q. Liu, Y.-G. Jiang, D. W. Zhang, M. Liu and P. Zhou, Two-Dimensional Materials for next-Generation Computing Technologies, *Nat. Nanotechnol.*, 2020, **15**(7), 545–557, DOI: 10.1038/s41565-020-0724-3.
2 J. Shim, H.-Y. Park, D.-H. Kang, J.-O. Kim, S.-H. Jo, Y. Park and J.-H. Park, Electronic and Optoelectronic Devices Based on Two-Dimensional Materials: From Fabrication to

Application, *Adv. Electron. Mater.*, 2017, **3**(4), 1600364, DOI: **10.1002/aelm.201600364**.

3 J. Li, X. Yang, Z. Zhang, W. Yang, X. Duan and X. Duan, Towards the Scalable Synthesis of Two-Dimensional Heterostructures and Superlattices beyond Exfoliation and Restacking, *Nat. Mater.*, 2024, 1–13, DOI: **10.1038/s41563-024-01989-8**.

4 M. A. Islam, E. Nicholson, N. Barri, M. Onodera, D. Starkov, P. Serles, S. He, B. Kumral, A. Zavabeti, H. Shahsa, T. Cui, G. Wang, T. Machida, C. V. Singh and T. Filleter, Strain Driven Electrical Bandgap Tuning of Atomically Thin WSe_2, *Adv. Electron. Mater.*, 2024, 2400225, DOI: **10.1002/aelm.202400225**.

5 M. Gastaldo, J. Varillas, Á. Rodríguez, M. Velický, O. Frank and M. Kalbáč, Tunable Strain and Bandgap in Subcritical-Sized MoS2 Nanobubbles, *Npj 2D Mater. Appl.*, 2023, **7**(1), 1–9, DOI: **10.1038/s41699-023-00432-x**.

6 T. Carey, O. Cassidy, K. Synnatschke, E. Caffrey, J. Garcia, S. Liu, H. Kaur, A. G. Kelly, J. Munuera, C. Gabbett, D. O'Suilleabhain and J. N. Coleman, High-Mobility Flexible Transistors with Low-Temperature Solution-Processed Tungsten Dichalcogenides, *ACS Nano*, 2023, **17**(3), 2912–2922, DOI: **10.1021/acsnano.2c11319**.

7 Z. Li, T. Zheng, M. Yang, Y. Sun, D. Luo, W. Gao, Z. Zheng and J. Li, A Dual Mode $MoTe_2/WS_2/WSe_2$ Double van der Waals Heterojunctions Phototransistor for Optical Imaging and Communication. Adv, *Opt. Mater.*, 2024, **12**(18), 2400023, DOI: **10.1002/adom.202400023**.

8 Achieving Ultrahigh Electron Mobility in PdSe2 Field-Effect Transistors *via* Semimetal Antimony as Contacts – Wang – 2023 – Advanced Functional Materials – Wiley Online Library. **https://onlinelibrary.wiley.com/doi/full/10.1002/adfm.202301651?casa_token=-nrcr9SQHr0AAAAA%3AI0x4Cd7PTgY6YI_MZYWD_9JJ2_v23q9_VuUIsvFL_O21G5SvaA5OF-ZfwklJm2I5A7CkJ17bk3sJA8UX5w** (accessed 2024-10-09).

9 E. Elahi, M. Rabeel, B. Ahmed, J. Aziz, M. Suleman, M. A. Khan, S. Rehman, A. Rehmat, M. Asim, M. A. Rehman, A. A. Ifseisi, M. E. Assal, M. F. Khan and S. Kim, Revealing Bipolar Photoresponse in Multiheterostructured WTe_2 – GaTe/$ReSe_2$ – WTe_2 P–N Diode by Hybrid 2D Contact Engineering, *ACS Appl. Mater. Interfaces*, 2024, **16**(40), 54367–54376, DOI: **10.1021/acsami.4c08166**.

10 Y. Zou, P. Li, C. Su, J. Yan, H. Zhao, Z. Zhang and Z. You, Flexible High-Temperature MoS2 Field-Effect Transistors and Logic Gates, *ACS Nano*, 2024, **18**(13), 9627–9635, DOI: **10.1021/acsnano.3c13220**.

11 Y. Zhang, X. Chen, M. Zhang, X. Wu, J. Wang, R. Tian, L. Fang, Y. Zhang, J. Zhao and X. Gan, Nonlinear Photodetector Based on InSe p–n Homojunction for Improving Spatial Imaging Resolution, *Adv. Funct. Mater.*, 2024, **34**(38), 2402957, DOI: **10.1002/adfm.202402957**.

12 Photo-controlled programmable logic gate *via* self-powered $Cu_2O/BiFeO_3/TiO_2$ ferroelectric heterojunction photodetectors – ScienceDirect. **https://www.sciencedirect.com/science/article/pii/S2211285524003513?casa_token=cZajn7qk4hcAAAAA:TwBja69mmmifsKwJ28O7jhubH6o_04Pih0sQIt5DH90_sNg8s68Q_RzSk2lu33ipppsg3kzqzKZu** (accessed 2024-10-10).

13 Mixed-Dimensional 1D/2D van der Waals Heterojunction Diodes and Transistors in the Atomic Limit|ACS Nano. **https://pubs.acs.org/doi/full/10.1021/acsnano.1c10524?casa_token=MUy3JEBiUucAAAAA%3Ax6gb5NM9Y7ABSyWDbGbpQzrhvWFQ4wnNpuEqLmUdVzF_aB4kJNasR6x0pR-Q69wMkbF94jLkLPmurzl1EA** (accessed 2024-10-10).

14 Vertically Stacked and Self-Encapsulated van der Waals Heterojunction Diodes Using Two-Dimensional Layered Semiconductors|ACS Nano, **https://pubs.acs.org/doi/10.1021/acsnano.7b05755** (accessed 2024-10-10).

15 S. Aftab, M. F. Khan, P. Gautam, H. Noh and J. Eom, MoTe2 van der Waals Homojunction p–n Diode with Low Resistance Metal Contacts, *Nanoscale*, 2019, **11**(19), 9518–9525, DOI: **10.1039/C8NR10526J**.

16 Type-I Transition Metal Dichalcogenides Lateral Homojunctions: Layer Thickness and External Electric Field Effects – Xia – 2018 – Small – Wiley Online Library. **https://onlinelibrary.wiley.com/doi/full/10.1002/smll.201800365** (accessed 2024-10-10).

17 2D Homojunctions for Electronics and Optoelectronics – Wang – 2021 – Advanced Materials – Wiley Online Library, **https://onlinelibrary.wiley.com/doi/full/10.1002/adma.202005303** (accessed 2024-10-10).

18 C.-S. Pang, C.-Y. Chen, T. Ameen, S. Zhang, H. Ilatikhameneh, R. Rahman, G. Klimeck and Z. Chen, WSe2 Homojunction Devices: Electrostatically Configurable as Diodes, MOSFETs, and Tunnel FETs for Reconfigurable Computing, *Small*, 2019, **15**(41), 1902770, DOI: **10.1002/smll.201902770**.

19 N. Shehzad, S. Saeed, I. Shahid, I. Khan, I. Saeed, J. A. Zapien and L. Zhang, Two-Dimensional van der Waals Heterostructures (vdWHs) with Band Alignment Transformation in Multi-Functional Devices, *RSC Adv.*, 2022, **12**(48), 31456–31465, DOI: **10.1039/D2RA03439E**.

20 Z. Wang and W. Zhu, Tunable Band Alignments in 2D Ferroelectric α-In2Se3 Based van der Waals Heterostructures, *ACS Appl. Electron. Mater.*, 2021, **3**(11), 5114–5123, DOI: **10.1021/acsaelm.1c00855**.

21 P. Tonndorf, R. Schmidt, P. Böttger, X. Zhang, J. Börner, A. Liebig, M. Albrecht, C. Kloc, O. Gordan, D. R. T. Zahn, S. M. Vasconcellos and R. Bratschitsch, Photoluminescence Emission and Raman Response of Monolayer MoS_2, $MoSe_2$, and WSe_2, *Opt. Express*, 2013, **21**(4), 4908–4916, DOI: **10.1364/OE.21.004908**.

22 Y.-H. Lee, L. Yu, H. Wang, W. Fang, X. Ling, Y. Shi, C.-T. Lin, J.-K. Huang, M.-T. Chang, C.-S. Chang, M. Dresselhaus, T. Palacios, L.-J. Li and J. Kong, Synthesis and Transfer of Single-Layer Transition Metal Disulfides on Diverse Surfaces, *Nano Lett.*, 2013, **13**(4), 1852–1857, DOI: **10.1021/nl400687n**.

23 Single flake homo p–n diode of $MoTe_2$ enabled by oxygen plasma doping, **https://www.degruyter.com/document/doi/10.1515/ntrev-2023-0207/html** (accessed 2024-09-23).

24 C. Tan, H. Wang, X. Zhu, W. Gao, H. Li, J. Chen, G. Li, L. Chen, J. Xu, X. Hu, L. Li and T. Zhai, A

Self-Powered Photovoltaic Photodetector Based on a Lateral WSe2-WSe2 Homojunction, *ACS Appl. Mater. Interfaces*, 2020, **12**(40), 44934–44942, DOI: **10.1021/acsami.0c11456**.

25 S. M. Sze, Y. Li and K. K. Ng, *Physics of Semiconductor Devices*, John Wiley & Sons, 2021.

26 C. J. Novotny, E. T. Yu and P. K. L. Yu, InP Nanowire/Polymer Hybrid Photodiode, *Nano Lett.*, 2008, **8**(3), 775–779, DOI: **10.1021/nl072372c**.

27 Z. Yuan, A Photodiode with High Rectification Ratio and Low Turn-on Voltage Based on ZnO Nanoparticles and SubPc Planar Heterojunction, *Phys. E*, 2014, **56**, 160–164, DOI: **10.1016/j.physe.2013.09.001**.

28 P. Pataniya, C. K. Zankat, M. Tannarana, C. K. Sumesh, S. Narayan, G. K. Solanki, K. D. Patel, V. M. Pathak and P. K. Jha, Paper-Based Flexible Photodetector Functionalized by WSe_2 Nanodots, *ACS Appl. Nano Mater.*, 2019, **2**(5), 2758–2766, DOI: **10.1021/acsanm.9b00266**.